

See discussions, stats, and author profiles for this publication at: <https://www.researchgate.net/publication/283696748>

Multiscale Effects of Interfacial Polymer Confinement in Silica Nanocomposites

ARTICLE *in* MACROMOLECULES · OCTOBER 2015

Impact Factor: 5.8 · DOI: 10.1021/acs.macromol.5b01111

READS

65

13 AUTHORS, INCLUDING:



Marius Mermet-Guyennet

5 PUBLICATIONS 3 CITATIONS

SEE PROFILE



Daniel Bonn

University of Amsterdam

254 PUBLICATIONS 7,117 CITATIONS

SEE PROFILE



Tobias Weidner

Max Planck Institute for Polymer Research

86 PUBLICATIONS 1,351 CITATIONS

SEE PROFILE



Sapun Parekh

Max Planck Institute for Polymer Research

40 PUBLICATIONS 903 CITATIONS

SEE PROFILE

Multiscale Effects of Interfacial Polymer Confinement in Silica Nanocomposites

H. Samet Varol,^{*,†} M. Alejandra Sánchez,[†] Hao Lu,[†] Joe E. Baio,[§] Christian Malm,[†] Noemi Encinas,[‡] Marius R. B. Mermet-Guyennet,^{||} Nicolas Martzel,[⊥] Daniel Bonn,^{||} Mischa Bonn,[†] Tobias Weidner,[†] Ellen H. G. Backus,[†] and Sapun H. Parekh^{*,†}

[†]Departments of Molecular Spectroscopy and [‡]Physics at Interfaces, Max Planck Institute for Polymer Research, Ackermannweg 10, 55128 Mainz, Germany

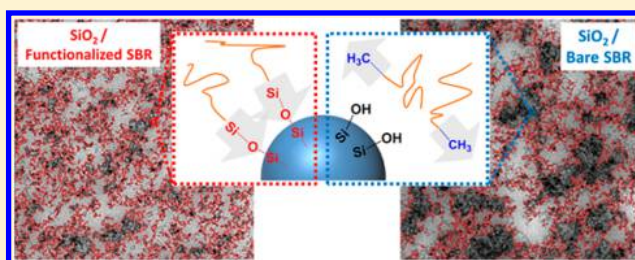
[§]School of Chemical, Biological and Environmental Engineering, Oregon State University, Corvallis, Oregon 97333, United States

^{||}Institute of Physics, University of Amsterdam, Science Park 904, 1098 XH Amsterdam, The Netherlands

[⊥]Manufacture française des pneumatiques MICHELIN, Site de Ladoux, 23 place Carmes Déchaux, 63040 Clermont-Ferrand, France

Supporting Information

ABSTRACT: Dispersing hydrophilic nanofillers in highly hydrophobic polymer matrices is widely used to tune the mechanical properties of composite material systems. The ability to control the dispersion of fillers is closely related to the mechanical tunability of such composites. In this work, we investigate the physical–chemical underpinnings of how simple end-group modification to one end of a styrene–butadiene chain modifies the dispersion of silica fillers in a polymer matrix. Using surface-sensitive spectroscopies, we directly show that polymer molecular orientation at the silica surface is strongly constrained for silanol functionalized polymers compared to nonfunctionalized polymers because of covalent interaction of silanol with silica. Silanol functionalization leads to reduced filler aggregation in composites. The results from this study demonstrate how minimal chemical modifications of polymer end groups are effective in modifying microstructural properties of composites by inducing molecular ordering of polymers at the surface of fillers.



INTRODUCTION

For many natural and synthetic composite materials, enhancing or reinforcing the linear and nonlinear viscoelastic properties of polymer (elastomer) materials is accomplished by inclusion filler particles (e.g., carbon black, silica).^{1–4} Mechanical properties of elastomer systems can be substantially increased, e.g., more than a 10-fold increase in shear modulus, by addition of fillers to the polymer matrix. Notably, this strengthening, or reinforcement, depends in a nontrivial manner on the distribution and size of fillers within the elastomer matrix.^{5–7} Interfacial interactions between individual particles in aggregates, between the aggregates in agglomerates, and between particles and the polymer can modulate particle dispersion and influence the molecular motion of polymer chains in the material. Moreover, in nanocomposites containing nanoparticle fillers with large surface area, the particle dispersion is a critical element for tuning optical,^{8,9} electrical,^{10–12} biological,^{13,14} and mechanical properties^{15–19} of the materials. Unfortunately, controlling the filler distribution in many popular nanocomposite formulations, such as SiO₂–particle reinforced rubber, is challenging because the typically highly hydrophilic fillers tend to aggregate in the hydrophobic host polymer melt. Previous approaches to overcome the hydrophobicity difference between the matrix and fillers include (1) covalent coupling of

the fillers to the polymer matrix using multifunctional molecules, for instance bis[3-(triethoxysilyl)propyl] tetrasulfide (TESPT),^{20–26} or (2) lowering the surface polarity of the hydrophilic fillers by surface modification with silanes,^{27–29} short hydrocarbons,^{30,31} or polymer layers grafted on the filler surface.³² A recently highlighted strategy for improving the dispersion of SiO₂ particles in styrene–butadiene rubber (SBR) is modifying the host SBR chains themselves with a single silanol functional group (Si–OH) at the end of the chain.^{33–35} The appealing part of this concept is that the aggregate size (R_{agg}) of SiO₂ fillers can be varied in styrene–butadiene rubber (SBR) by simply changing the concentration of functionalized SBR (F-SBR) chains in the total SBR matrix. However, the impact of polymer functionality on polymer–filler interaction—if any—is still unclear because of the complexity in previously studied systems and inability to investigate the polymer–substrate physicochemical properties.³⁴

In this work, we investigate the influence of a single Si–OH end functional group on 50% of total SBR chain ends on polymer–silica interaction at the molecular level by studying

Received: May 22, 2015

Revised: October 9, 2015

well-defined systems with a combination of microscopy and surface-sensitive spectroscopy. We evaluate the adhesion and molecular ordering of both F-SBR and nonfunctionalized or bare SBR (B-SBR) polymers to SiO₂ surfaces. Our spectroscopic results demonstrate preferential adhesion of F-SBR chains to SiO₂ surfaces and directly show enhanced ordering of polymer chains in F-SBR-SiO₂ films compared with B-SBR-SiO₂ from surface specific sum frequency generation and near-edge X-ray absorption fine structure spectroscopy. Finally, depth-resolved X-ray photoelectron spectroscopy was used to show that the Si–OH group formed a covalent bond with OH-terminated silicon surfaces. The multiscale effect of using the Si–OH functionalized SBR starts with covalent interaction between F-SBR and SiO₂ fillers that leads to increased polymer ordering and ultimately manifests as improved filler distribution and reduced aggregation at the microscopic level compared to B-SBR–SiO₂ composites.

MATERIALS AND METHODS

Materials. For all composites fabricated in this study, we used nonvulcanized/non-crosslinked styrene butadiene rubber (SBR) polymers. Two types of SBR polymers were employed: 1) silanol end-functionalized SBR (F-SBR) and 2) bare SBR (B-SBR) polymers. Both polymers were synthesized in Michelin laboratories.³⁴ Initiation of anionic polymerization of both random F-SBR and B-SBR copolymers are done by using *n*-BuLi in a methylcyclohexane. *N*-(1,3-dimethylbutyl)-*N'*-phenyl-*p*-phenylenediamine and 4,4'-methylene-bis-2,6-*tert*-butylphenol were used as antioxidants during the polymerization of both copolymers. Protic terminating agent was used to terminate the B-SBR polymerization. Termination of the F-SBR polymerization was obtained by reaction with hexamethylcyclotrisiloxane in order to have silanol end group at one end of each F-SBR chain. Functionalized end-group of F-SBR can be chemically written as SBR–SiMe₂–OH. Functional group fraction in one end of all F-SBR chains was reported previously as greater than 98% according to the results from ¹H and ²⁹Si NMR.³⁴ In the same previous paper, microstructures of both polymers are also shown similar to each other due to their identical polymerization steps. Each chain of both copolymers statistically consists of 26 wt % of styrene and 74 wt % of butadiene units (41 wt % of 1,2-butadiene and 59 wt % of 1,4-butadiene units).³⁴ These subunits are indicated in every molecular structure shown in the paper by using the letters m, n, k and p for styrene, 1,2-butadiene and 1,4-butadiene (*k*+*p*, for *trans* and *cis*), respectively. However, the ratio of [*1,4*]_{trans} to [*1,4*]_{cis} or *k*:*p* ratio is not known, and it is not crucial for the content of this paper as it is the same for B-SBR and F-SBR. Gel permeation chromatography (GPC) of the polymer showed the *M_n* and polydispersity index (PDI) of both stock polymer solutions in THF (*M_n*~150–160 kDa, PDI~1.08–1.11) to be very similar to each other, and very close to values previously reported for identical SBR polymers.³⁴ The polymer chain stock solutions (40 mg/mL THF) were prepared by dissolving bulk slabs of B-SBR and F-SBR in THF for 4 days at 4 °C. The 4-day incubation time was necessary to completely solubilize the polymers in THF.

Fumed Silica nanofillers (Aerosil 200, Evonik, *R₀* = 6 nm) were used as received to prepare a stock solution. Silica particles were prepared as a stock solution (15.2 mg/mL THF) by ultrasonic dispersion of the nanoparticles with a probe-type sonicator (half inch probe diameter, 10 s, 60% amplitude, inside of an ice-bath) at room temperature.

Nanocomposite Formulation. Formulation details of the full nanocomposites can be found elsewhere.³⁴ Simplified nanocomposites were prepared according to the following protocol. Silica fillers at a concentration of 45 per hundred rubber (PHR) or 16 % volume fraction of nanofillers were mixed with the polymer solution. 5.920 mL nanofiller stock solution was added to 5 mL of polymer chain stock solution. The final mixture was mixed with an ultrasonic tip (half inch probe diameter) for 10 s at 60% amplitude while sitting in an ice bath. After mixing, initial THF removal was done by rotary evaporation under 20 mbar for 30 min (Rotavapor R-200, Buechi, Essen). Complete THF removal was done by keeping the samples in a vacuum oven at 80 °C for 24 h. In order to prevent reaction between end-functional Si–OH of F-SBR and the surface of any glassware, we used only plastic ware for all the simplified nanocomposite sample preparations.

Transmission Electron Microscopy Imaging and Image Processing. All nanocomposite samples were sectioned to a thickness of 50 nm by ultracryotome (LEICA EM UC6, Wetzlar) at –60 °C using a diamond knife (Cryotome ultra 35°, Hatfield, USA) for the transmission electron microscopy (TEM) imaging. TEM micrographs were taken by operating a JEOL electron microscope (JEOL JEM 1400, Echling) with an accelerating voltage of 120 kV with constant electron beam intensity and at a magnification of 5000X. We imaged a total 4000 aggregates/sample from different locations within each section to compute the average aggregate size of the nanofillers (*R_{agg}*). The aggregates were determined by applying a thresholding routine to highlight silica aggregates against the rubber background in each TEM image using ImageJ. The following steps were followed: 1) OK Brightness and Contrast, 2) unsharp mask (radius was set to 45 and mask weight was used as 0.6), 3) threshold with a value of the difference value between mean and stdDev of each image, which can be found in histogram after the step 2, and 4) counting (from one primary filler to infinite size). This procedure was kept constant for all samples measured.

The output from the image analysis was: aggregate projected area (*A*), perimeter, and centroid location. We assume a circular shape with the measured projected area (*A*) for each aggregate from which we calculated the aggregate radius (*R_{agg}*).

Statistical Analysis of Image Data. Statistical analyses from image processing were done with OriginPro using the ANOVA package. Aggregates from different fields-of-view for the same material (section) were grouped together, and the ANOVA procedure allows us to compare the variance in aggregate size for each sample to test if the mean value is statistically different from the other samples. The comparison test performed was Tukey, and significant differences between two samples are shown by a black asterisk, indicating a *P* value < 0.05.

Contact Angle Measurements. Teflon and silica window substrates were first cleaned by immersing in piranha solution (3:1 (v/v) H₂SO₄: H₂O₂) for 10 min then rinsed with milli Q water and absolute ethanol. The substrates were then left in a desiccator for 24 h for complete drying. Spin coating of the B-SBR and F-SBR films on Teflon and silica window surfaces were done by using a spin coating device Model WS-400-6NPP/LITE (Laurel Technologies Corp., North Wales, USA). 100 μL from each 40 mg/mL stock solutions of F-SBR and B-SBR were deposited on the substrates during 1 min at 3000 rpm. After the spin coating, the substrates with polymer films on the top were left in desiccator for 24 h.

For understanding a possible polarity difference between the B-SBR and F-SBR due to polymer functionality, we measured the contact angle of water as probe liquid on aforementioned spin coated polymer films on the top of Teflon or silica windows. The contact angle experiments were performed with an OCA35 goniometer (DataPhysics, Germany). The advancing contact angle of the spun coated rubber films was evaluated by placing an initial sessile droplet of milli Q water of 5 μL on the surfaces. The volume of the deposited droplet was increased up to 25 μL at a rate of 0.5 $\mu\text{L/s}$ while keeping the needle in the drop. At the plateau regions of the contact angle (CA) in increasing volume the advancing CA for water of the polymer films is obtained. Advancing CA presented in Figure S7 are reported after averaging the mean values from at least two different spot per spin coated film and three different plateaus (cycles) per each of these spots.

Drop Cast Polymer Film Preparation and Characterization. Drop cast films of pure F-SBR or B-SBR were prepared for various spectroscopy measurements in this study, and the following method was used, 1500 μL from each 40 mg/mL of polymer stock solutions were drop cast on cleaned IR-transparent silica windows (Infrasil, International Crystal Laboratories, Garfield). Windows were cleaned by following the previously mentioned piranha cleaning protocol of the substrates for before the spin coating.

Teflon rings were used as molds for film casting. The drop cast polymer films were kept inside a fume hood for 1 h before being transferred to a vacuum desiccator for 24 h in order to obtain THF-free polymer films. After complete removal of the THF from the polymer, the residual dry film thickness was found to be 150 μm –180 μm by measurement with a microscope (IX81, Olympus, Tokyo) using a 40X, NA 0.75 objective lens (Olympus, Tokyo).

Infrared Spectroscopy. Fourier transform infrared spectroscopy (FTIR) was used to measure characteristic peaks of the residual polymer films adhered to a piranha-cleaned silicon wafers and absorption of IR light by polymer films on silica windows. Samples were measured with a Nicolet 730 FTIR spectrometer. All FTIR spectra shown were averaged over three different regions of the drop cast film. The integration time for the IR measurements was 800 s. Average IR intensity values between the frequencies of 2120 cm^{-1} and 2140 cm^{-1} of each averaged FTIR spectra were used for the background subtraction.

Sum-Frequency Generation Spectroscopy. Sum frequency generation (SFG) experiments were performed on the silica-polymer interface of drop-cast polymer films with broadband SFG system in the following way. 1.7 mJ of energy from a Ti:sapphire regenerative amplifier (Spitfire Ace, Spectra-Physics; 800 nm, 5 mJ, 1 kHz, ~ 40 fs) was used to pump a commercial optical parametric amplifier (Topas-C, Spectra-Physics). This resulted in 4 μJ infrared (IR) pulses centered at 3000 cm^{-1} with a full width at half maximum (FWHM) of ~ 400 cm^{-1} . Visible narrow band pulses with a center wavelength of 800 nm and FWHM of ~ 15 cm^{-1} were obtained by passing part of the 800 nm laser output through an etalon (SLS Optics Ltd). The IR and visible beams were spatially and temporally overlapped on a film sample with incident angles of $\sim 30^\circ$ (visible) and $\sim 40^\circ$ (IR) with respect to the surface normal. The energy of the visible and IR pulses at the sample were 5 μJ and 3 μJ , respectively, to avoid sample damage. The reflected SFG signal was directed to a spectrograph (Acton Instruments) and detected with an electron-multiplied charge-

coupled device (EMCCD) camera (Newton; Andor Technologies). Spectra were recorded using Andor Solis software with an integration time of 10 min. All spectra were collected under SSP polarization (s-polarized SFG, s-polarized visible, p-polarized infrared).

SFG Data Analysis. The SFG signal results from a second-order nonlinear interaction, which is only non-zero in non-centrosymmetric media. This makes SFG especially useful to probe interfacial phenomena where the interface between two media clearly breaks the symmetry, and a finite SFG signal is generated that reflects the molecular composition and structure of the interface. The SFG intensity is proportional to the square of the second order nonlinear susceptibility $\chi^{(2)}$ of the sample and the visible and infrared electric fields

$$I_{\text{SFG}} = |E_{\text{SFG}}|^2 \propto |\chi^{(2)} E_{\text{VIS}} E_{\text{IR}}|^2 \quad (1)$$

The SFG is enhanced when the frequency of the incident infrared field is resonant with a vibrational mode present at the interface. The susceptibility $\chi^{(2)}$ consists of a resonant (RES) and nonresonant (NR) term

$$\chi^{(2)} = \chi_{\text{NR}}^{(2)} + \chi_{\text{RES}}^{(2)} = A_{\text{NR}} e^{i\phi_{\text{NR}}} + \sum_n \frac{A_n}{\omega_{\text{IR}} - \omega_n + i\Gamma_n} \quad (2)$$

where A_{NR} is the amplitude of the nonresonant susceptibility, ϕ_{NR} the phase, A_n the amplitude of the n th resonance with frequency ω_n , and Γ_n the line width of the vibrational transition. To correct for the spectral shape of the IR pulse, data were normalized to a reference spectrum from a 100-nm evaporated gold layer on IR-transparent silica. Equation 2 was then used to fit the normalized SFG spectra and extract the peak amplitudes and positions for the different resonances. The Maximum Entropy Method for phase retrieval was used to verify the phase of the peaks and the non-resonant signal.⁴⁶ All SFG spectra shown in this work are an average of 12 spectra (four spots on two independent samples).

Near-Edge X-Ray Absorption Fine Structure (NEXAFS) Microscopy. Near-edge X-ray absorption fine structure (NEXAFS) microscopy was performed on the silica-polymer interface of drop-cast polymer films; however, before placing the drop cast polymer films in the NEXAFS analysis chamber, the bulk polymer layer was peeled off the silica window by using a fine tweezer. This was done in order to analyze the thin polymer film in close proximity to the silica surface.

NEXAFS images were collected at the U7 beamline at the National Synchrotron Light Source (NSLS - Brookhaven National Laboratory). An X-ray beam, with energy scanned around the carbon K-edge was raster scanned across an 18×13 mm^2 area on the sample. The spatially resolved partial electron yield (PEY) was measured using a rapid imaging analytical tool (LARIAT, Synchrotron Research Inc.). The step size for the scans was 0.1 eV (2 s dwell time). The emitted photoelectrons were guided to an electron yield detector by a full field imaging parallel magnetic field. This produced a series of NEXAFS images with a 50 μm spatial resolution, which was used for the small spot analysis of different areas of the films. The spectra shown are representative of four spots analysed on the sample surface. To eliminate the effect of incident beam intensity fluctuations and absorption features in the beamline optics, the PEY was normalized by the drain current signal of a clean gold mesh located upstream of the analysis chamber along the path of the incident X-ray beam. All the images and spectra from

NEXAFS analysis in this paper have been pre- and post-edge normalized using the Athena software package.

Ultrathin Spun Coat Polymer Film Preparation and X-Ray Photoelectron Spectroscopy. For the XPS measurements, 20 μL drops from each 10 mg/mL F-SBR/THF and B-SBR/THF solutions were deposited onto piranha cleaned Si wafers. These Si wafers with polymer solution drops on the top were then spin coated for 60 s at 3000 rpm. After the spin coating, the samples were kept under vacuum and then they placed inside of the XPS ultra high vacuum chamber. The approximate thickness of the spin coat polymer films was determined using a KLA Tencar P-16 stylus profiler (KLA Tencar, Milpitas, California). XPS was conducted using a Kratos Axis Ultra spectrometer (Kratos, Manchester, England) using an Al K α excitation source with a photon energy of 1487 eV. An argon gas cluster ion source (GCIS) was used for depth profiling the atomic composition of the polymer films (Figure S5). The sputter source was set to a raster size of 1.5 mm \times 1.5 mm, and \sim 200 etching steps were required to fully remove the 60 nm polymer film.

The data was acquired in small spot mode (0.1 mm spot diameter) using a 0° take-off angle, defined as the angle between the surface normal and the axis of the analyzer lens. The analyzer pass energy was set to 80 eV for composition analysis. The molecular environment of the samples was probed by high-resolution spectra (analyzer pass energy = 20 eV) from the C1s and O1s regions. The charge neutralizer was always used during spectra collection (filament current 1.8 Å, charge balance 2 V, and filament bias 1.3 V). The binding energy scales were calibrated to the main bulk Si 2p emission at 99.3 eV, and a linear background was subtracted for all peak quantifications. The peak areas were normalized by the manufacturer supplied sensitivity factors and surface concentrations were calculated using the Kratos Vision software.

RESULTS AND DISCUSSION

Silanol Functional End Groups on Polymer Chains Modify SiO₂ Filler Aggregation. The molecular structures of the two styrene–butadiene (SBR) polymers used in this work are shown in Figure 1c (inset). The synthesis of the two polymers has been described previously, and the basic protocol is summarized in the Methods.³⁴ The only difference between the two polymers is a single silanol (Si–OH) end group on “functionalized” SBR (F-SBR), corresponding to 1 Si–OH at the end of an \sim 150 g mol^{−1} SBR chain. The other polymer, with terminal methyl groups, will further be referred to as “bare” SBR (B-SBR). In complex, industrial silica-filled composites, F-SBR chains have been shown to substantially affect silica nanofiller aggregation and distribution.^{33,34} This difference is purported to occur via interaction of the Si–OH on the polymer to the silica surface, which creates a brush around fillers to reduce the filler–filler aggregation. This hypothesis is in line with previous studies that have shown that grafting of polymer chains on silica surfaces reduces filler aggregation in hydrophobic environments.²⁴ However, explaining the origin of changing nanofiller dispersions in SBR as a result of polymer functionality alone is not obvious in complex industrial formulations. They include many additional ingredients, e.g. TESPT, octyltriethoxysilane (OCTEO), additional (proprietary) oils, and antioxidants, all of which can influence particle dispersion.^{33,34}

To isolate the effect of silanol end-functional groups on filler aggregation in silica-loaded SBR composites, we begin by

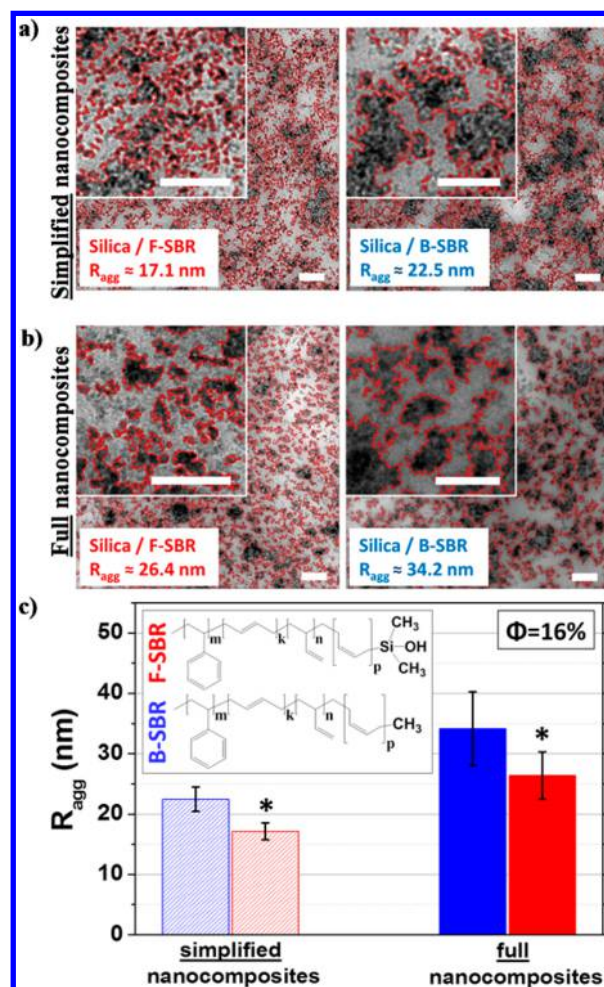


Figure 1. TEM images of (a) simplified nanocomposites, which consist of only nanoparticles inside polymer matrices and (b) the full nanocomposites (see ref 35 for detailed ingredients in addition to polymer chains and silica nanoparticles). Red outlines demarcate the borders of each aggregate after image analysis. All samples contain 16 vol % of silica fillers in B-SBR or F-SBR. Scale bars are 200 nm. (c) Average aggregate sizes (R_{agg}) of simplified and full nanocomposites. Red and blue bars represent R_{agg} of samples with F-SBR and B-SBR polymeric matrices, respectively. The inset shows the molecular structures of the two polymers. Letters, m, k, n, and p represent the amounts of statistically ordered polymer units of both random copolymers (see Methods for the details). Histograms of the aggregate sizes of all the composites are presented as Supporting Information (Figure S2). Asterisks denote statistically significant differences ($p < 0.05$) of R_{agg} between B-SBR–silica and F-SBR–silica samples (1-way ANOVA with Tukey’s). Error bars are standard errors of mean.

analyzing the size distribution of silica aggregates (R_{agg}) in simplified nanocomposite systems. These composites contain only the polymer (F-SBR or B-SBR) and silica nanofillers (see Methods). Transmission electron microscopy (TEM) images of ultrathin sections (\sim 50 nm) of simplified nanocomposite systems were acquired and processed to identify aggregates (dark contrast regions, see Methods for details) dispersed in the polymeric matrix (Figure 1a). For comparison purposes, full nanocomposites were also imaged and processed to identify aggregates (Figure 1b). We quantified the effective aggregate radius R_{agg} of each different composite by averaging the area of 4000 aggregates from each composite and assuming a circular shape, similar to what is done in small-angle X-ray scattering.

Figure 1c shows that in both full and simplified nanocomposites samples containing F-SBR (red bars) have smaller aggregates than those with B-SBR (blue bars). We note that while TEM is certainly not the optimal choice for analysis of nanoscale aggregates in polymer matrices, we have compared our results with those from small-angle X-ray scattering (SAXS) for full nanocomposite systems and find reasonable agreement at 16 % volume fraction with more dispersity at 24 % volume fraction (Figure S1). The thresholding step in our image analysis is subject to the image contrast between polymer and fillers (see Methods), and because the distance between aggregates decreases at higher filler volume fraction, this makes absolute aggregate size quantification less accurate at higher volume fraction. Furthermore, interpretation of aggregate sizes as a function of volume fraction is difficult as competing effects (e.g., particle shearing and energetically driven aggregation) can oppositely affect the aggregate size, and disentangling these effects is challenging.^{34,36,37} Nevertheless, the consistent reduction of aggregate size seen in F-SBR composites compared to B-SBR composites from both TEM image analysis and SAXS for 16% and 24% volume fraction filler demonstrates that our quantitative aggregate analysis is robust for comparing aggregate sizes at the same volume fraction with different polymer matrices (Figure S1). Thus, our results show that in both full and simplified composites a single Si–OH end-functional group on an SBR polymer chain is able to modify the aggregation behavior of silica nanofillers in composite systems.

Silanol Functional End Group Enhances Polymer Chain Attachment on SiO₂ Surfaces. To better understand the origin of the aggregate size decrease in silica/F-SBR samples, we compared the adhesion of B-SBR and F-SBR polymers with planar SiO₂ surfaces. Polymers were drop-cast onto piranha-cleaned silicon wafers from a stock solution of polymer in THF (see Methods). Cleaned silicon wafers typically have a thin (SiO₂) oxide layer after piranha cleaning.^{38–40} We tested if Si–OH groups on the F-SBR polymer increased attachment to the wafers by rinsing the polymer-coated wafers in a THF bath for 80 s. Since the polymers were initially dissolved in a THF solution, rinsing with THF should solubilize weakly adhered polymer chains in both B-SBR and F-SBR films. After this procedure, a visible film was left on the wafer coated with F-SBR, but no film was observed on the B-SBR-coated wafer (Figure 2a). We subsequently used Fourier transform infrared spectroscopy (FTIR) to determine the chemical composition of the residual film on the F-SBR coated silicon wafer. Representative spectra from the THF-washed wafers are shown in Figure 2b. These spectra confirm the presence of SBR after THF rinsing for the drop-cast F-SBR film while no chemical moieties (beyond those of the Si wafer) were apparent for the corresponding B-SBR sample. From these data, we conclude that attachment of the F-SBR polymer to the piranha-cleaned silicon wafer is clearly enhanced by the single Si–OH group on the chains.

Molecular Ordering of Polymer Chains on SiO₂ from Silanol Functional End Group Interaction with SiO₂ Surfaces. The enhanced attachment of F-SBR chains on silicon surfaces presumably originates from the Si–OH group interacting with the SiO₂. We further explored the surface–polymer interaction to determine if any differential molecular orientation was induced by Si–OH mediated attachment of the F-SBR polymer to silica. Vibrational sum frequency generation (SFG) spectroscopy and near-edge X-ray absorption fine

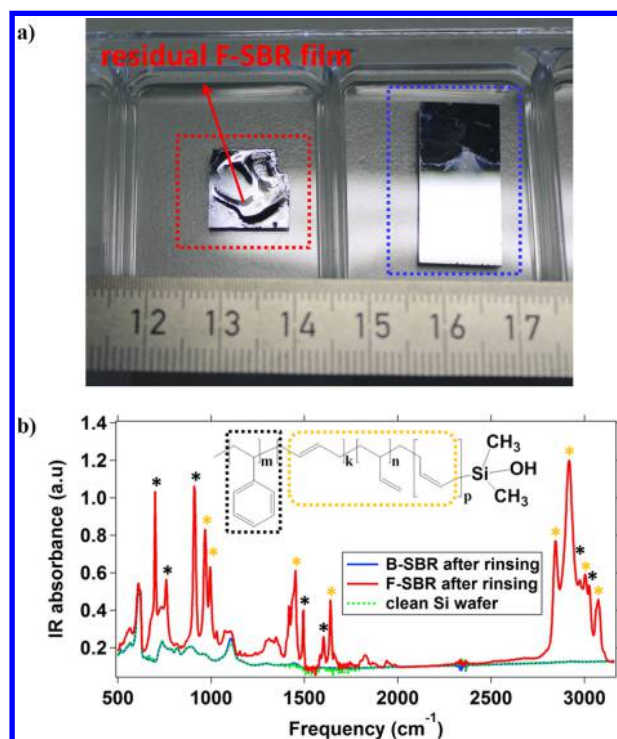


Figure 2. (a) Photographic images of F-SBR (left) and B-SBR (right) residue on silicon wafers after rinsing polymer films with THF. (b) FTIR spectra of residual films on Si wafer after rinsing in THF. Clear peaks from SBR are observed for the F-SBR polymer (red) while only Si wafer peaks (green-dashed) are seen after the B-SBR polymer (blue) has been rinsed. Characteristic groups of SBR are shown by outlines in yellow or black on the chemical structure. The same colors are used to identify particular vibrations (marked by asterisks) in the spectrum associated with each characteristic group.

structure (NEXAFS) spectroscopy were used to measure molecular order of the polymer at the silica surface.

SFG is a second-order nonlinear vibrational spectroscopy that relies on frequency mixing of an infrared with a visible laser pulse to generate light with the sum frequency. The SFG intensity is strongly enhanced when the infrared laser wavelength is resonant with molecular moieties (e.g., CH₂, C=C, or Si–CH₃ groups) that are present and noncentrosymmetrically oriented at an interface. SFG has a typical probing depth of ~2–3 molecular layers⁴¹ and has been used extensively to characterize polymer films on various interfaces,^{42–47} making this technique well-suited for our system. For SFG (and NEXAFS) experiments, we used drop-cast films of B-SBR and F-SBR on cleaned, infrared-grade silica windows—without THF washing. Silica windows were used instead of wafers because visible light transparency is required for SFG experiments.

SFG spectra were collected from the silica window surface–polymer interface by passing the laser beams through the silica to the silica–polymer interface as shown in Figure 3a. In principle, polymer SFG signals should come from both the polymer–silica and polymer–air interfaces. However, in these samples the polymer–air SFG signal is negligible because the infrared light in the CH region is strongly absorbed by the drop-cast polymer layer (see Figure S3), so SFG is only detected from the polymer–silica interface. SFG spectra were recorded under SSP polarization conditions (s-polarized SFG, s-polarized visible and p-polarized IR).

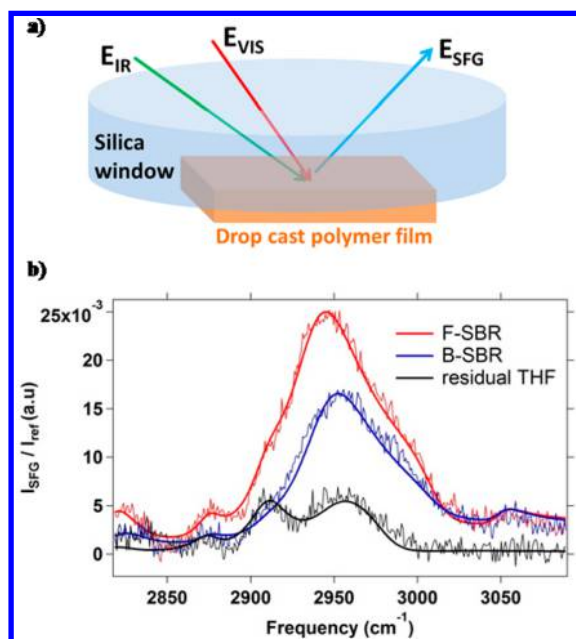


Figure 3. (a) Schematic illustration of the SFG measurements of drop-cast polymer films on IR-transparent silica. Two incoming photons (infrared and visible shown by green and red arrows, respectively) are spatially and temporally overlapped at the window–polymer interface and generate a photon (E_{SFG} , shown by the blue arrow) with the sum of these frequencies. (b) Normalized (by a reference spectrum from a gold-coated window) SFG spectra measured from F-SBR (red) and B-SBR (blue) and residual THF without polymer (black). Thick lines are fits to the spectra based on a standard model (see Methods).

Figure 3b shows the SFG spectra from the F-SBR–silica interface in red and the B-SBR–silica interface in blue. Spectra from both polymers indicate some degree of molecular order at the silica interface as evidenced by the peaks in the spectra. Control spectra from a THF solution dried on the silica window (without any polymer) showed a 300% and 500% decrease in intensity at $\sim 2950\text{ cm}^{-1}$ compared to B-SBR and F-SBR, respectively (Figure 3b, black).

The spectra from the F-SBR–silica interface shows clear deviation from the B-SBR–silica interface at ~ 2915 and 2950 cm^{-1} , in addition to a larger overall amplitude. In order to assign peak frequencies and identify the specific moieties contributing to the spectra, we fit the SFG data with a standard model explained in the Methods (using parameters that can be found in Table S1). The fitting results are also depicted in Figure 3b (thick lines) and show good agreement with the acquired data. The robustness of the fit was further demonstrated by comparing the reconstructed resonant spectra from the fits with the extracted resonant spectra via the commonly used maximum entropy method (MEM) analysis (Figure S4).⁴⁸ These two independent analyses show similar spectra, underscoring the accuracy of the fits to allow reliable peak assignment.

From the fitting results and previous work on polymer–glass interfaces for polydimethylsiloxane (PDMS) in contact with silica, we can identify likely resonances in the SFG spectra. The PDMS–silica interface shows symmetric and asymmetric Si–CH₃ vibrations at roughly 2915 and 2960 cm^{-1} .⁴⁹ Similarly, we assign the 2910 cm^{-1} shoulder and 2940 cm^{-1} peak in the F-SBR spectrum to these two Si–CH₃ vibrations (Figure 3b, red). In the B-SBR–silica sample, the broad signal at 2945 cm^{-1} possibly originates from the CH₃ end group; however, a

definitive assignment is not possible. Nevertheless, the identity of the peaks (Si–CH₃) in the F-SBR–silica system and the overall larger intensity (compared to B-SBR) show that the Si–OH group in F-SBR is in close proximity to the silica and stabilizes a conformation of the polymer in which the neighboring Si–CH₃ groups exhibit a noncentrosymmetric organization.

As a complementary technique to SFG, NEXAFS spectroscopy allows one to determine the spatial orientation of chemical structures based on absorption of a polarized X-ray beam by the sample.^{50,51} NEXAFS spectra were measured on the same type of drop-cast films as used for SFG measurements. Prior to introducing the samples into the NEXAFS analysis chamber, the bulk drop-cast polymer layers were physically ripped from the silica window, leaving behind a residual polymer film on the SiO₂ surface (Figure 4a).

NEXAFS spectroscopy probes the molecular structure of surface adsorbed species by measuring characteristic absorption resonances corresponding to electronic transitions from atomic core levels to unoccupied molecular orbitals.⁵¹ Carbon K-edge spectra from randomly chosen regions of interest of B-SBR and F-SBR residues on silica windows, acquired at 70° and 30° relative to the incident X-ray beam, are presented in Figure 4b. The absorption at 285.4 eV , from π^* C=C orbitals, is present in all spectra taken from both types of polymers.^{52,53} Moving to higher X-ray energies, we observe a shoulder at 288 eV and a broad resonance at 293 eV related to $\text{R}^*/\text{C}-\text{H}\sigma^*$ and C–C σ^* molecular orbitals, respectively.^{53–56}

Preferential orientation of molecular bonds was investigated by subtracting spectra from 70° and 30° tilt angles. Difference spectra ($70^\circ - 30^\circ$) from B-SBR and F-SBR residual films are shown in Figure 4c. A comparison of the two difference spectra (Figure 4c) shows a substantially higher degree of order (positive dichroism) for the π^* C=C feature for the F-SBR polymer residue interfaced with silica with a peak height of 0.2 at 285.2 eV . No significant dichroism was observed for the B-SBR residue–SiO₂ interface, especially in the π^* C=C region of the difference spectrum (5-fold lower than for F-SBR). This shows that the functionalization of the SBR polymer with a single Si–OH induces a specific orientation of C=C double bonds, such that the C=C bonds are somewhat upright relative to the substrate.

Covalent Nature of the Interfacial Interaction between Silanol Functional End Groups and Silica. Our results show decreased silica aggregation, enhanced adhesion, and enhanced molecular ordering of F-SBR polymers at silica interfaces, relative to B-SBR polymers, as a result of the presence of the Si–OH end functional group on the F-SBR polymer. However, none of the above measurements have addressed the question how the Si–OH group interacts with silica: chemisorption or physisorption. In order to address this question, we studied the elemental composition and chemical state of the B-SBR and F-SBR polymer films spun-cast onto piranha-cleaned Si wafers using depth-resolved X-ray photoelectron spectroscopy (XPS). Spin-coated polymer films (thickness $\sim 60\text{ nm}$) were depth profiled by repeated sputtering using an argon cluster source and XPS analysis of the exposed surface (see Methods and Figure S5). This process provides a snapshot of atomic concentrations (%) at different depths in the polymer film as it is etched toward the substrate. By plotting the atomic concentration of Si and C versus etch time, we can define a particular etching period that best reflects the polymer–substrate interface (Figure S5).

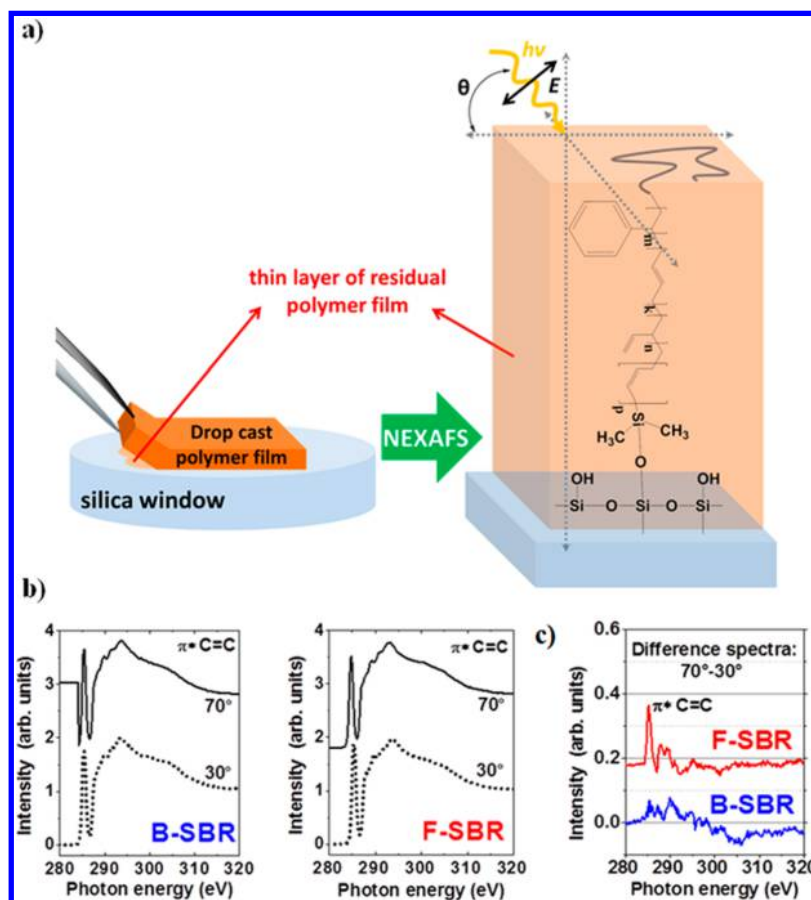


Figure 4. (a) Illustration showing removal of drop-cast polymer films using tweezers before the NEXAFS measurements. Silica windows with the residual polymer film were introduced into the NEXAFS analysis chamber. Preferential orientation of molecules (e.g., π^* C=C orbitals within SBR chain) to the silica surface can be determined from changes in X-ray absorption at different sample rotation (θ) relative to the incident X-rays. (b) Carbon K-edge spectra extracted from random regions of B-SBR (left) and F-SBR (right) residual films on silica acquired at 70° (straight lines) and 30° (dotted lines). (c) The difference spectra (70° - 30°) are shown in red and blue for F-SBR and B-SBR, respectively. Spectra in (b) and (c) were vertically offset for clarity.

The C 1s spectra of both F-SBR and B-SBR at the SiO₂ layer (which is present after piranha etching silicon) show a main emission near 285.3 eV assigned to aliphatic and aromatic CC bonds (Figure 5a).^{57–59} Spectral fitting reveals that the spectra for the F-SBR–SiO₂ interface contain a second peak near 286.4 eV, which can be assigned to C–Si–O or Si–C bonds coming from the Si–OH end functional groups at the end of F-SBR chains.^{60–63} This additional peak supports the conclusion from SFG that the Si–OH end functional groups are condensed at polymer–Si wafer interface and not in the bulk film (Figure S6a). Looking next at the corresponding O 1s spectra of both polymers at SiO₂ layer, we observe a common peak at 531.8 eV originating from Si–O bonds at the Si wafer surface.^{64,65} Similar to the C 1s spectra, we identified an additional peak after fitting the O 1s spectrum for F-SBR (Figure 5b). The second peak near 533.7 eV can be assigned to Si–O–R and Si–O–Si bonds^{61,64,66} and appears only at the F-SBR–silica interface—not in the bulk film (Figure S6b).

This observation is corroborated by the Si 2p spectra shown in Figure 5c. The main spectral features near 104.4 and 99.3 eV in both spectra related to Si–O–Si species within the thin oxide layer^{66–69} are accompanied by a peak near 102.7 eV—only in the F-SBR spectra. The latter peak can be assigned to C–Si–O–Si.^{60,64,68,70} Together, the additional peaks from C 1s (286.4 eV), O 1s (533.7 eV), and Si 2p (102.7 eV) spectra at

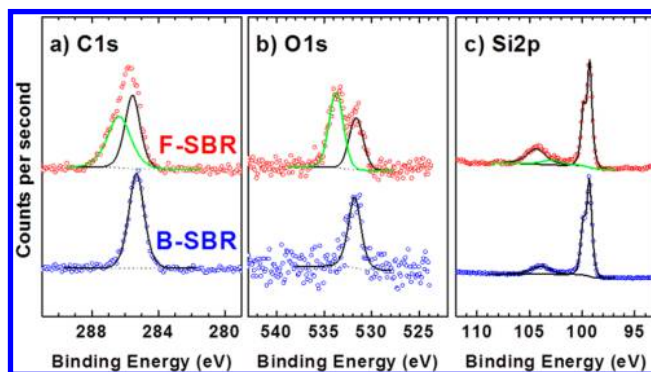


Figure 5. XPS spectra of the (a) C 1s, (b) O 1s, and (c) Si 2p from the polymer–wafer interface along with fit results (see Methods for details) collected from the F-SBR (red) and B-SBR (blue) films. Argon cluster etching time for the B-SBR–Si wafer interface is between 180 and 360 s. The F-SBR–Si wafer interface XPS results were extracted from etching times between 210 and 390 s. Figure S5 shows atomic % for C 1s, O 1s, and Si 2p during the entire argon etching times for both polymer samples. In all the XPS spectral fits, green and black lines are additional and common peaks, respectively, for both polymers.

the polymer–substrate interface led us to the following conclusions: (i) the (CH₃)₂–Si–OH end functional groups of F-SBR chains are enriched at the surface of the Si wafer and

not detectable in the bulk film and (ii) the formation of chemical bonds between the Si–OH group and the silicon substrate, which leads to the formation of $(\text{CH}_3)_2\text{Si–O–Si}$ moieties at the interface as the result of a condensation reaction.

CONCLUSION

In this work, we demonstrate that single Si–OH end groups on SBR chains are sufficient to enhance the interaction of SBR chains with silicon and SiO_2 . The increased interaction manifests as stronger adhesion of the F-SBR chains to silicon surfaces as compared to B-SBR chains. Together with increased adhesion, the additional interaction of the Si–OH functionalized polymer with SiO_2 fillers ultimately led to reduced aggregation of the silica nanofillers within the SBR matrix. The fact that the simplified and full composites showed similar reduced aggregation in F-SBR compared to B-SBR polymers suggests polymer–filler interactions also contribute to improving the dispersion of fillers in the more complex melt formulations as well. The idea of grafting polymer chains to silica particle surfaces with end group modifications has been previously demonstrated, though in the context of hydrophilic polymers, to study polymer segmental motion at silica interfaces.^{71–73} This is quite different from the current study in which a hydrophobic rubber—SBR—was attached to silica using a terminal silanol group, which allows identification of functional (aggregation) and physical chemical (molecular ordering) differences when compared to methyl-terminated SBR.

To further explore the molecular origin of the improved adhesion of F-SBR chains to glass surfaces, we employed multiple surface-specific spectroscopies. From these measurements, we observed strong dichroism in carbon K-edge spectra from NEXAFS showing ordering of $\text{C}=\text{C}$ bonds in the F-SBR/silica system. Further experiments with SFG showed that the F-SBR–silica interfaces exhibited Si– CH_3 signals that were larger than in B-SBR films. Finally, XPS spectra showed covalent bonding of Si–OH groups with silicon substrates in F-SBR films. These findings, along with the polymers having identical hydrophobicity (Figure S7), show that interaction of a single Si–OH group from the F-SBR polymer with the SiO_2 filler surface results in polymer ordering at the silica surface, which thereby decreases filler aggregation in the nanocomposites. While it is possible that specific, covalent attachment of polymers to an interface can cause disorder in the case of multivalent attachment, the combined results from SFG and NEXAFS surface spectroscopies for F-SBR films demonstrate that covalently attached polymers are more ordered at the silica interface.^{74,75} The results from this study provide a mechanistic basis for future attempts to directly graft hydrophobic host polymer matrices to hydrophilic fillers with aim of improving filler dispersion and mechanical properties of composite materials.

ASSOCIATED CONTENT

Supporting Information

The Supporting Information is available free of charge on the ACS Publications website at DOI: 10.1021/acs.macromol.5b01111.

Supporting figures; Figures S1–S7 (PDF)

AUTHOR INFORMATION

Corresponding Authors

*E-mail varol@mpip-mainz.mpg.de (H.S.V.).

*E-mail parekh@mpip-mainz.mpg.de (S.H.P.).

Notes

The authors declare no competing financial interest.

ACKNOWLEDGMENTS

We acknowledge I. Lieberwirth, G. Glaser, and K. Kirchoff for assistance with TEM imaging and ultracryotome sample preparation. M.A.S. thanks the Max Planck Graduate Center for funding. This work is part of the research programme ‘Understanding the viscoelasticity of elastomer based nanocomposites’ (I1VEC01) of the ‘Stichting voor Fundamenteel Onderzoek der Materie (FOM)’, which is financially supported by the ‘Nederlandse Organisatie voor Wetenschappelijk Onderzoek (NWO)’.

REFERENCES

- (1) Ben Azouz, K.; Ramires, E. C.; Van Den Fonteyne, W.; El Kissi, N.; Dufresne, A. *ACS Macro Lett.* **2012**, *1*, 236–240.
- (2) McNally, T.; Pötschke, P.; Halley, P.; Murphy, M.; Martin, D.; Bell, S. E. J.; Brennan, G. P.; Bein, D.; Lemoine, P.; Quinn, J. P. *Polymer* **2005**, *46*, 8222–8232.
- (3) Sapkota, J.; Jorfi, M.; Weder, C.; Foster, E. J. *Macromol. Rapid Commun.* **2014**, *35*, 1747–1753.
- (4) Sternstein, S. S.; Zhu, A. J. *Macromolecules* **2002**, *35*, 7262–7273.
- (5) Jancar, J.; Douglas, J.; Starr, F. *Polymer* **2010**, *51*, 3321–3343.
- (6) Kalfus, J.; Jancar, J. *Polymer* **2007**, *48*, 3935–3937.
- (7) Mermet-Guyennet, M. R. B.; Gianfelice de Castro, J.; Varol, H. S.; Habibi, M.; Hosseinkhani, B.; Martzel, N.; Sprick, R.; Denn, M. M.; Zacccone, A.; Parekh, S. H.; Bonn, D. *Polymer* **2015**, *73*, 170–173.
- (8) Oberdisse, J. *Soft Matter* **2006**, *2*, 29.
- (9) Jones, B. A.; Facchetti, A.; Marks, T. J.; Wasielewski, M. R. *Chem. Mater.* **2007**, *19*, 2703–2705.
- (10) Winey, K. I.; Vaia, R. A. *MRS Bull.* **2007**, *32*, 314–319.
- (11) Schadler, L. S.; Kumar, S. K.; Benicewicz, B. C.; Lewis, S. L.; Harton, S. E. *MRS Bull.* **2007**, *32*, 335–340.
- (12) Moniruzzaman, M.; Winey, K. I. *Macromolecules* **2006**, *39*, 5194–5205.
- (13) Rooney, M. M.; Farrell, D. H.; van Hemel, B. M.; de Groot, P. G.; Lord, S. T. *Blood* **1998**, *92*, 2374–2381.
- (14) Lam, W. A.; Chaudhuri, O.; Crow, A.; Webster, K. D.; Li, T.-D.; Kita, A.; Huang, J.; Fletcher, D. A. *Nat. Mater.* **2011**, *10*, 61–66.
- (15) Heinrich, G.; Klüppel, M.; Vilgis, T. A. *Curr. Opin. Solid State Mater. Sci.* **2002**, *6*, 195–203.
- (16) Guth, E. J. *Appl. Phys.* **1945**, *16*, 20.
- (17) McCarthy, D. W.; Mark, J. E.; Clarkson, S. J.; Schaefer, D. W. *J. Polym. Sci., Part B: Polym. Phys.* **1998**, *36*, 1191–1200.
- (18) Dewimille, L.; Bresson, B.; Bokobza, L. *Polymer* **2005**, *46*, 4135–4143.
- (19) Payne, A. R. *J. Appl. Polym. Sci.* **1965**, *9*, 2273–2284.
- (20) Akcora, P.; Kumar, S. K.; Moll, J.; Lewis, S.; Schadler, L. S.; Li, Y.; Benicewicz, B. C.; Sandy, A.; Narayanan, S.; Ilavsky, J.; Thiagarajan, P.; Colby, R. H.; Douglas, J. F. *Macromolecules* **2010**, *43*, 1003–1010.
- (21) Chevigny, C.; Dalmas, F.; Di Cola, E.; Gigmes, D.; Bertin, D.; Boué, F.; Jestin, J. *Macromolecules* **2011**, *44*, 122–133.
- (22) Chevigny, C.; Jouault, N.; Dalmas, F.; Boué, F.; Jestin, J. *J. Polym. Sci., Part B: Polym. Phys.* **2011**, *49*, 781–791.
- (23) Akcora, P.; Liu, H.; Kumar, S. K.; Moll, J.; Li, Y.; Benicewicz, B. C.; Schadler, L. S.; Acehan, D.; Panagiotopoulos, A. Z.; Pryamitsyn, V.; Ganesan, V.; Ilavsky, J.; Thiagarajan, P.; Colby, R. H.; Douglas, J. F. *Nat. Mater.* **2009**, *8*, 354–359.
- (24) Kumar, S. K.; Jouault, N.; Benicewicz, B.; Neely, T. *Macromolecules* **2013**, *46*, 3199–3214.

- (25) Castellano, M.; Conzatti, L.; Costa, G.; Falqui, L.; Turturro, A.; Valenti, B.; Negroni, F. *Polymer* **2005**, *46*, 695–703.
- (26) Hasegawa, R.; Aoki, Y.; Doi, M. *Macromolecules* **1996**, *29*, 6656–6662.
- (27) Meth, J. S.; Zane, S. G.; Chi, C.; Londono, J. D.; Wood, B. A.; Cotts, P.; Keating, M.; Guise, W.; Weigand, S. *Macromolecules* **2011**, *44*, 8301–8313.
- (28) Zhang, Q.; Archer, L. A. *Langmuir* **2002**, *18*, 10435–10442.
- (29) Aranguren, M. I.; Mora, E.; Macosko, C. W. *J. Colloid Interface Sci.* **1997**, *195*, 329–337.
- (30) Harms, S.; Rätzke, K.; Faupel, F.; Schneider, G. J.; Willner, L.; Richter, D. *Macromolecules* **2010**, *43*, 10505–10511.
- (31) Nusser, K.; Neueder, S.; Schneider, G. J.; Meyer, M.; Pyckhout-Hintzen, W.; Willner, L.; Radulescu, A.; Richter, D. *Macromolecules* **2010**, *43*, 9837–9847.
- (32) Radhakrishnan, B.; Ranjan, R.; Brittain, W. J. *Soft Matter* **2006**, *2*, 386.
- (33) Baeza, G. P.; Genix, A.-C.; Degrandcourt, C.; Gummel, J.; Couty, M.; Oberdisse, J. *Soft Matter* **2014**, *10*, 6686–6695.
- (34) Baeza, G. P.; Genix, A.; Degrandcourt, C.; Petitjean, L.; Schweins, R.; Couty, M.; Oberdisse, J. *Macromolecules* **2013**, *46*, 6621–6633.
- (35) Baeza, G. P.; Genix, A.; Degrandcourt, C.; Petitjean, L. *Macromolecules* **2013**, *46*, 317–329.
- (36) Kotsilkova, R.; Fragiadakis, D.; Pissis, P. *J. Polym. Sci., Part B: Polym. Phys.* **2005**, *43*, 522–533.
- (37) Baeza, G. P.; Genix, A. C.; Degrandcourt, C.; Gummel, J.; Mujtaba, A.; Saalwächter, K.; Thurn-Albrecht, T.; Couty, M.; Oberdisse, J. *ACS Macro Lett.* **2014**, *3*, 448–452.
- (38) In, I.; La, Y.; Park, S.; Nealey, P. F.; Gopalan, P. *Langmuir* **2006**, *22*, 7855–7860.
- (39) Yam, C.; Xiao, Z.; Gu, J.; Boutet, S.; Cai, C. *J. Am. Chem. Soc.* **2003**, *125*, 7498–7499.
- (40) Leontis, I.; Othonos, A.; Nassiopoulou, A. G. *Nanoscale Res. Lett.* **2013**, *8*, 383.
- (41) Nagata, Y.; Mukamel, S. *J. Am. Chem. Soc.* **2010**, *132*, 6434–6442.
- (42) Wang, J.; Even, M. A.; Chen, Z. *Macromolecules* **2002**, *35*, 8093–8097.
- (43) Loch, C. L.; Wang, J.; Chen, Z. *J. Phys. Chem. B* **2003**, *107*, 10440–10445.
- (44) Loch, C. L.; Ahn, D.; Chen, C.; Wang, J.; Chen, Z. *Langmuir* **2004**, *20*, 5467–5473.
- (45) Wang, J.; Chen, C.; Buck, S. M.; Chen, Z. *J. Phys. Chem. B* **2001**, *105*, 12118–12125.
- (46) Wang, J.; Paszti, Z.; Even, M. A.; Chen, Z. *J. Am. Chem. Soc.* **2002**, *124*, 7016–7023.
- (47) Chen, Z.; Shen, Y. R.; Somorjai, G. A. *Annu. Rev. Phys. Chem.* **2002**, *53*, 437–465.
- (48) Sovago, M.; Vartiainen, E.; Bonn, M. *J. Phys. Chem. C* **2009**, *113*, 6100–6106.
- (49) Zhang, C.; Chen, Z. *J. Phys. Chem. C* **2013**, *117*, 3903–3914.
- (50) Baio, J. E.; Jaye, C.; Fischer, D. A.; Weidner, T. *Anal. Chem.* **2013**, *85*, 4307–4310.
- (51) Stöhr, J. *NEXAFS Spectroscopy*; Springer Science & Business Media: Berlin, 1992.
- (52) Himmel, H.-J.; Terfort, A.; Wöll, C. *J. Am. Chem. Soc.* **1998**, *120*, 12069–12074.
- (53) Outka, D. A.; Stöhr, J.; Rabe, J. P.; Swalen, J. D. *J. Chem. Phys.* **1988**, *88*, 4076.
- (54) Väterlein, P.; Fink, R.; Umbach, E.; Wurth, W. *J. Chem. Phys.* **1998**, *108*, 3313.
- (55) Weiss, K.; Bagus, P. S.; Wöll, C. *J. Chem. Phys.* **1999**, *111*, 6834.
- (56) Baio, J. E.; Weidner, T.; Brison, J.; Graham, D. J.; Gamble, L. J.; Castner, D. G. *J. Electron Spectrosc. Relat. Phenom.* **2009**, *172*, 2–8.
- (57) Afzal, A.; Siddiqi, H. M.; Saeed, S.; Ahmad, Z. *RSC Adv.* **2013**, *3*, 3885.
- (58) Gulino, A.; Lupo, F.; Fragalà, M. E.; Schiavo, S. L. *J. Phys. Chem. C* **2009**, *113*, 13558–13564.
- (59) Puniredd, S. R.; Assad, O.; Haick, H. *J. Am. Chem. Soc.* **2008**, *130*, 13727–13734.
- (60) Liu, Z. C.; He, Q. G.; Xiao, P. F.; Liang, B.; Tan, J. X.; He, N. Y.; Lu, Z. H. *Mater. Chem. Phys.* **2003**, *82*, 301–305.
- (61) Shao, Y. X.; Dong, D.; Cai, Y. H.; Wang, S.; Ang, S. G.; Xu, G. Q. *J. Phys. Chem. C* **2010**, *114*, 17159–17165.
- (62) Roghani-Mamaqani, H.; Haddadi-Asl, V. *Polym. Int.* **2014**, *63*, 1912–1923.
- (63) Sengupta, R.; Chakraborty, S.; Bandyopadhyay, S.; Dasgupta, S.; Mukhopadhyay, R.; Auddy, K.; Deuri, A. S. *Polym. Eng. Sci.* **2007**, *47*, 21–25.
- (64) Mani, G.; Johnson, D. M.; Marton, D.; Dougherty, V. L.; Feldman, M. D.; Patel, D.; Ayon, A. A.; Mauli Agrawal, C. *Langmuir* **2008**, *24*, 6774–6784.
- (65) Armstrong, J. L. *J. Vac. Sci. Technol., A* **1998**, *16*, 123.
- (66) Li, S. H.; Zhu, X. F.; Zhao, Y. P. *J. Phys. Chem. B* **2004**, *108*, 17032–17041.
- (67) Schildenberger, M.; Prins, R.; Bonetti, Y. C. *J. Phys. Chem. B* **2000**, *104*, 3250–3260.
- (68) Azoune, A.; Carpi, N.; Fink, J.; Chehimi, M. M.; Cuvelier, D.; Piel, M. *Langmuir* **2011**, *27*, 7349–7352.
- (69) Vanden Eynde, X.; Servais, J. P.; Lamberigts, M. *Surf. Interface Anal.* **2003**, *35*, 1004–1014.
- (70) Kannan, A. G.; Choudhury, N. R.; Dutta, N. K. *Polymer* **2007**, *48*, 7078–7086.
- (71) Glomann, T.; Schneider, G. J.; Allgaier, J.; Radulescu, A.; Lohstroh, W.; Farago, B.; Richter, D. *Phys. Rev. Lett.* **2013**, *110*, 1–5.
- (72) Glomann, T.; Hamm, A.; Allgaier, J.; Hübner, E. G.; Radulescu, A.; Farago, B.; Schneider, G. J. *Soft Matter* **2013**, *9*, 10559.
- (73) Kim, S. Y.; Meyer, H. W.; Saalwächter, K.; Zukoski, C. F. *Macromolecules* **2012**, *45*, 4225–4237.
- (74) Weidner, T.; Krämer, A.; Bruhn, C.; Zharnikov, M.; Shaporenko, A.; Siemeling, U.; Träger, F. *Dalton Trans.* **2006**, 2767–2777.
- (75) Glebe, U.; Weidner, T.; Baio, J. E.; Schach, D.; Bruhn, C.; Buchholz, A.; Plass, W.; Walleck, S.; Glaser, T.; Siemeling, U. *ChemPlusChem* **2012**, *77*, 889–897.